Luminescent and Ferromagnetic CdS:Mn^{2+}/C Core−Shell Nanocrystals

Sayan Bhattacharyya,*,† Y. Estrin,‡ D. H. Rich,‡ D. Zitoun,§,|| Yuri Koltypin,§ and A. Gedanken*,§

Department of Chemical Sciences, Indian Institute of Science Education and Research, Kolkata, Mohanpur-741252, Nadia, W.B., India, Department of Physics, The Ilse Katz Institute for Nanoscience and Nanotechnology, Ben-Gurion University of the Negev, P.O. Box 653, Beer-Sheva 84105, Israel, Department of Chemistry and Kanbar Laboratory for Nanomaterials at the Bar-Ilan University Center for Advanced Materials and Nanotechnology, Bar-Ilan University, Ramat-Gan 52900, Israel, and ICGM-AIME, Université Montpellier II, CC15, Place Bataillon 34095, Montpellier, France

Received: July 29, 2010; Revised Manuscript Received: November 14, 2010

The Mn-doped CdS nanocrystals encapsulated by carbon ($Cd_{1-x}Mn_xS$/C) were synthesized by a one-step, kinetically controlled, solid-state reaction under autogenic pressure at elevated temperatures. The ∼50 nm wurtzite $Cd_{1-x}Mn_xS$ core was encapsulated by a 5−11 nm disordered carbon shell, and with the increase in Mn concentration, a gradual change from isotropic nanocrystals to one-dimensional nanorods was observed. Electron paramagnetic resonance studies showed that Mn^{2+} could be efficiently doped into the CdS lattice up to a Mn:Cd atomic ratio of 0.012. The 0.9−1.8 atomic % manganese-doped CdS samples were found to be ferromagnetic at room temperature, and the magnetic moment did not saturate even at 2 K, likely due to the coexistence of superparamagnetic fractions and antiferromagnetic coupling between the Mn^{2+} spins. The lowest-doped samples (Mn:Cd = 0.009 and 0.012) display the highest magnetic moments (4.43 ± 0.04 and 4.52 ± 0.04 μ_B/Mn), respectively. The more concentrated samples exhibit weaker magnetic moments (2.85 ± 0.03 μ_B/Mn for Mn:Cd = 0.018) as a result of antiferromagnetic coupling between Mn^{2+} second neighbors. Cathodoluminescence spectroscopy experiments were performed from 50 to 300 K to assess the temperature dependence of emissions related to the CdS near band edge, the Mn intra d-shell $^4T_1 \rightarrow {}^6A_1$ transition, defect-related surface state transitions, and the effect of surface passivation with carbon. The temperature-dependent spectral line shape variations, the emission intensities, and energies of the various components were examined for each Mn doping density to evaluate the incorporation of Mn^{2+} into the host CdS nanocrystal lattice.

Introduction

Diluted magnetic semiconductor (DMS) systems, where magnetic ions randomly substitute the host semiconductor cations, are among the most significant present-day nanomaterials because of their potential use in electronic devices.[1] To integrate the DMS materials into electronic devices, it is important to have low-dimensional structures in order to gain advantages offered by the spins. Manganese-doped cadmium sulfide (CdS) nanocrystals have been widely studied in this regard for a range of applications.[2] In fact, CdS, being a semiconductor with a room-temperature direct band gap of 2.42 eV is a useful candidate for applications, such as light-emitting diodes, photoconductors, solar cells, thin film transistors, and green lasers.[3] However, doping magnetic ions inside the semiconductor host lattice is always controversial due to the incompatibility of dopants with the host lattice and difficulty of the "surface adsorption" of impurities on the nanocrystal surface.[4] The extent of efficient doping definitely depends on the synthesis methods employed, where a control is needed to ascertain the concentration and location of dopants in the nanocrystal ensemble. Doping is only possible when lattice incorporation and diffusion of the dopant ions overcome the "self-purification" process.

Mn-doped CdS DMS materials have been realized in the form of nanocrystals inside a glass matrix,[5] thin films,[3] and nanocrystals coated with semiconductors, such as CdS and ZnS[2b,6] or silica.[7] The surface properties of the nanocrystals have a significant effect on the structural and optical properties because a large surface-to-volume ratio results in a significant portion of the atoms and doped ions being located on or near the surface of the nanocrystals. The surface states are likely to trap electrons/holes, inducing nonradiative recombinations and reduction of luminescence efficiency.[2c] The surface chemistry of luminescent II−VI semiconductors and DMS nanocrystals has been extensively studied to reduce the surface-related defects and improve performance of the nanodevices.[2b,c,6b,8] The most discussed surface-coating approach is to create heterostructures in the form of core−shell nanostructures, where the shell consists of either a wider band-gap semiconductor with minimal lattice mismatch[2b] or organic biocompatible species.[9] The inorganic semiconductor shell provides efficient and photostable nanocrystals, which are bioincompatible and toxic, whereas the biocompatible organic capping molecules are usually distorted in shape, bulky in size, and atomically mismatch the nanocrystal surface, resulting in partial coverage.[2c]

Considering the pros and cons of the various capping agents, a nanometric carbon shell is the best bet in terms of having a much lower molecular mass and size, and biocompatible nature. Carbon is well known to be a successful coating material to

* To whom correspondence should be addressed. E-mail: sayanb@iiserkol.ac.in (S.B.), gedanken@mail.biu.ac.il (A.G.).
† Indian Institute of Science Education and Research.
‡ Ben-Gurion University of the Negev.
§ Bar-Ilan University.
|| Université Montpellier II.

10.1021/jp107083f
Published on Web 11/30/2010

increase biocompatibility of inorganic nanostructures for biological/biomedicinal applications.[10] Carbon is so effective in protecting the properties of the nanocrystal core that even prolonged exposure of a high-energy electron beam does not diminish the luminescence intensity below 10−15%, after which the intensity saturates.[11,12] In this paper, Mn^{2+}-doped CdS nanocrystals encapsulated by a carbon shell were synthesized, and the efficiently doped CdS:Mn^{2+} nanocrystals were found to be ferromagnetic at room temperature and highly luminescent. The carbon shell was formed by an in situ one-step, solid-state, kinetically controlled reaction under autogenic pressure and elevated temperatures, unlike the lengthy procedures followed for other coating materials. Large-scale production of the nanocrystals is possible by increasing the amount of the precursors and the size of the reactor. The structural, magnetic, and optical properties of the nanocrystals are discussed. The optical properties have been studied with variable-temperature cathodoluminescence (CL). The incorporation of Mn^{2+} into the host nanocrystal was assessed by examining variations in the CdS near band edge (NBE), the Mn^{2+} intra d-shell $^4T_1 \rightarrow {}^6A_1$ transition, and defect-related surface state transitions. The data were analyzed with fits using multiple Gaussian components to quantify changes in luminescence intensity and energy of the various components for each sample as the temperature was varied. Details regarding the temperature dependence of recombination and relaxation kinetics were inferred from this analysis.

Experimental Section

Cadmium acetate dihydrate [$C_4H_6O_4Cd \cdot 2H_2O$, Aldrich, 98%], manganese(II) acetate tetrahydrate [$C_4H_6O_4Mn \cdot 4H_2O$, Fluka, >99%] and sulfur powder [Aldrich, 99.99%] were used as received. All the reactants were handled inside a N_2-filled

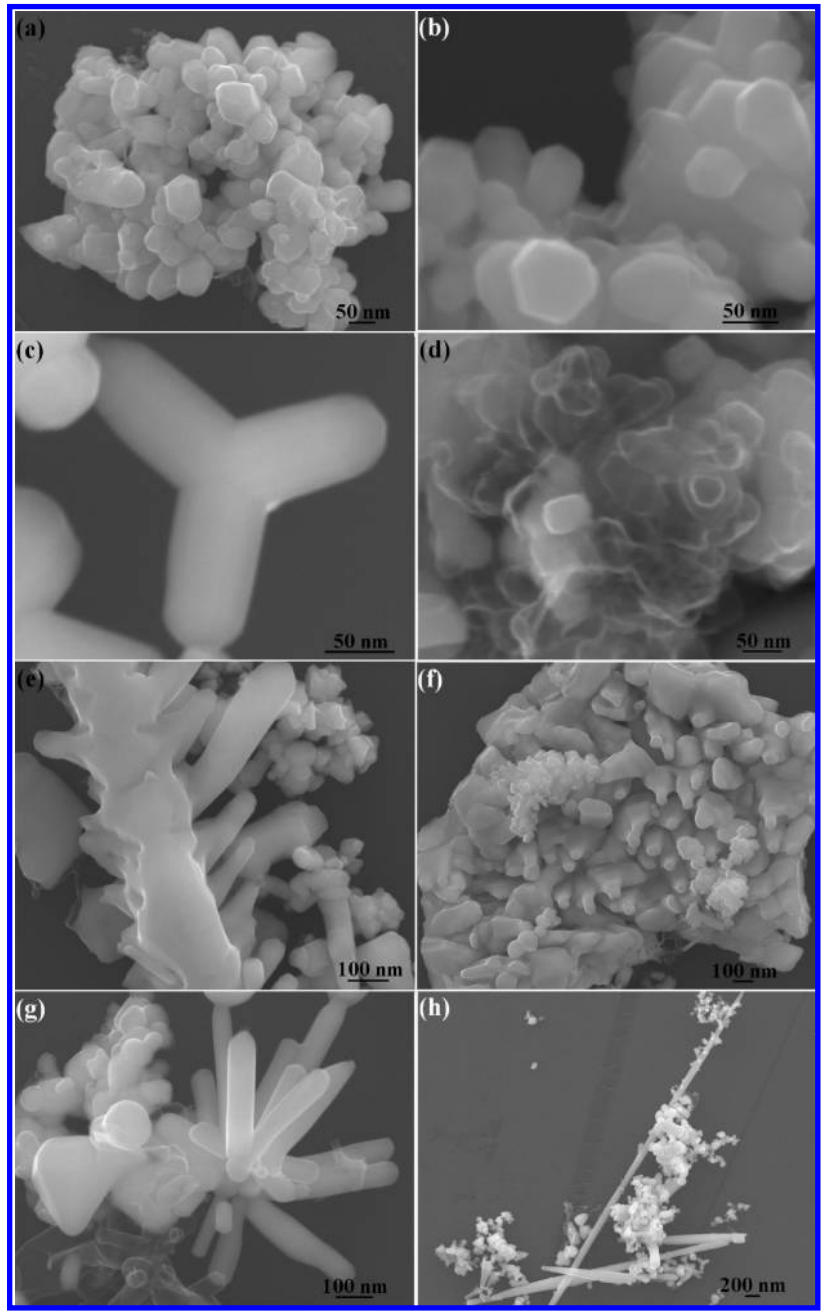

Figure 1. HRSEM images of the nanocrystals of (a) C0 and (b) C1, (c) a single tripod of C2, (d) carbon shells in C2, (e) treelike nanobranches of C3, (f) C4 nanobranches at the formation stage, and nanorods of (g) C4 and (h) C5.

glovebox. In a typical synthesis of Mn-doped CdS nanostructures encapsulated with carbon, 3 g of $C_4H_6O_4Cd \cdot 2H_2O$, 0.4 g of S, and a stoichiometric amount of $C_4H_6O_4Mn \cdot 4H_2O$ (according to the Mn:Cd atomic ratios of 0−0.05) were mixed and filled inside a quartz tube fitted within a 5 mL stainless steel reactor, sealed on one end. The reactor filled with precursors was tightly sealed at the other end and heated in a tube furnace at 10 °C min^{-1}, maintained at 800 °C for 4 h. The reactor was cooled (∼5 h) to ambient temperature. The dry grayish powder was sonicated in ethanol for 30 min and dried under vacuum after decanting the dark liquid from the top to remove the contaminant carbonaceous species. The bare CdS:Mn^{2+} nanocrystals were synthesized using a previously reported method.[15]

The obtained products were structurally characterized using a high-resolution scanning electron microscope (HRSEM, JSM, 7000F), a transmission electron microscope (TEM, JEOL, 2010), powder X-ray diffraction (Cu Kα = 1.5418 Å radiation, Bruker AXS D8), inductively coupled plasma atomic emission spectroscopy (ICP-AES, Spectroflame Module E), and energy-dispersive X-ray spectroscopy (EDS, JEOL, 2010). An Olympus BX41 (Jobin-Yvon-Horiba) Raman spectrometer was employed, using the 514.5 nm line of an Ar ion laser as the excitation source to analyze the nature of the core, as well as that of the carbon shell. The electron paramagnetic resonance (EPR) spectrum was recorded on a Bruker EPR spectrometer (ER083 CS) operating at an X-band (ν = 9.77 GHz) with a 100 kHz magnetic field modulation. Magnetic properties were measured using a Super Quantum Interference Design (SQUID) magnetometer MPMS XL7, in the temperature range of 2−300 K and fields varying between 0 and 5 T. The temperature-dependent susceptibility was measured using a dc procedure. The sample was cooled to 2 K under a zero magnetic field. A low magnetic field (5 mT) was applied, and data were collected from 2 to 350 K (zero-field-cooled, ZFC). Field-cooled (FC) measurements were performed from 2 to 300 K with an applied field during the cooling. The cathodoluminescence (CL) experiments were performed with a modified JEOL-5910 scanning electron microscope (SEM) using a 15 keV electron beam with a probe current of 2.5 nA. The electron beam was rapidly rastered over a 64 μm × 48 μm region of each sample to yield spectra representative of the average emission for nanocrystals in each sample. A UV multialkali photomultiplier tube (PMT) operating in the 185−850 nm spectral range enabled photon counting of the luminescence that was dispersed by a 0.25-m monochromator. Measurements were performed at different temperatures in the 50−300 K temperature range.[16]

Results and Discussion

Structural Characterization. The synthesis of the nanocrystals was carried out with the commercially available solid-state precursors inside a quartz tube fitted in a disposable cell to guarantee the lack of any contamination. An approximate 80% yield of the nanocrystal products was determined, and inductively coupled plasma (ICP) experiments revealed the overall bulk composition of the solid products. Accordingly we designate to the Mn:Cd atomic ratios of 0, 0.009, 0.012, 0.018, 0.024, and 0.045 the symbols C0, C1, C2, C3, C4, and C5, respectively, in subsequent discussions in the paper. The corresponding Mn weight percentages are 0.43 (C1), 0.62 (C2), 0.90 (C3), 1.2 (C4), and 2.3 (C5). However, the aforementioned compositions are not meant to suggest that all Mn^{2+} ions are substitutionally doping the host CdS nanocrystal. ICP analysis did not detect any contamination, such as iron or nickel, from the stainless steel reactor in any of the powders. The carbon

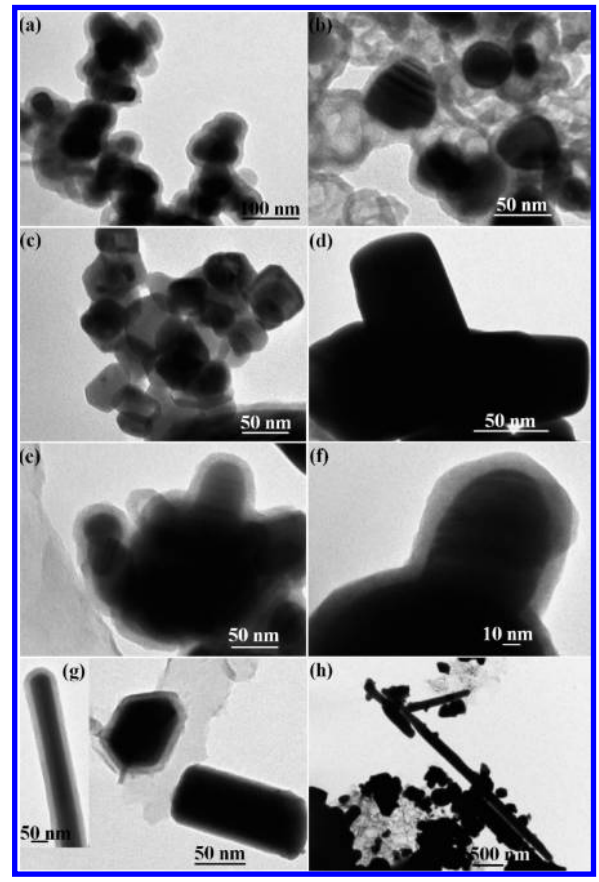

Figure 2. Bright-field TEM images of the nanocrystals of (a) C0, (b) C1, and (c) C2. TEM images of the one-dimensional nanostructures: (d) tripod of C2, (e) nanobranches in C3, (f) nanorod of C3, (g) C4 nanocrystals and a single core−shell nanorod (inset), and (h) a mixture of isotropic nanocrystals and nanorods in C5.

weight percentages as determined from C, H, N analysis are 20.9, 21.5, 20.7, 21.5, 20.6, and 19.9 for C0, C1, C2, C3, C4, and C5, respectively. Morphological changes were observed as a function of the Mn/Cd atomic ratio from the high-resolution SEM/TEM images for the prepared products. Figure 1 shows the HRSEM images of the products, and the nanocrystals are found to gradually change from being spherical to one-dimensional with the increase in Mn concentration. For C0 and C1, the nearly hexagonally shaped isotropic particles are 51 ± 7 and 52 ± 9 nm, respectively. Tripod nanostructures start to grow in C2, the branches of the tripod being 65 ± 2 nm, coexisting with the isotropic nanocrystals. The isolated carbon shells were observed in most of the samples, and Figure 1d shows the 37 ± 6 nm carbon nanostructures for C2. One-dimensional nanostructures were observed with a Mn concentration of 0.9% (C3) and higher. In C3 (Figure 1e), 71 ± 7 nm treelike nanobranches were observed, whereas in C4 (Figure 1f), some nanobranches were at the incomplete formation stage, protruding out of a common base. Fully grown C4 nanorods are observed in Figure 1g, where the dimension of the nanorods are D = 65 ± 6 nm and L = 400−500 nm. With 3.1% Mn in C5, higher aspect ratio nanorods (D = 130 ± 15 nm and L ≃ 4.2 μm) were observed to coexist with the spherical nanocrystals. It is highly probable that manganese catalyzes the formation of the one-dimensional nanobranches and nanorods, the aspect ratio and percentage of which increase with higher Mn/Cd atomic ratios. Unfortunately, the carbon shell is not prominent in the HRSEM images. However, the TEM images in Figure 2 clearly demonstrates the core−shell morphology of the $Cd_{1-x}Mn_xS$/C

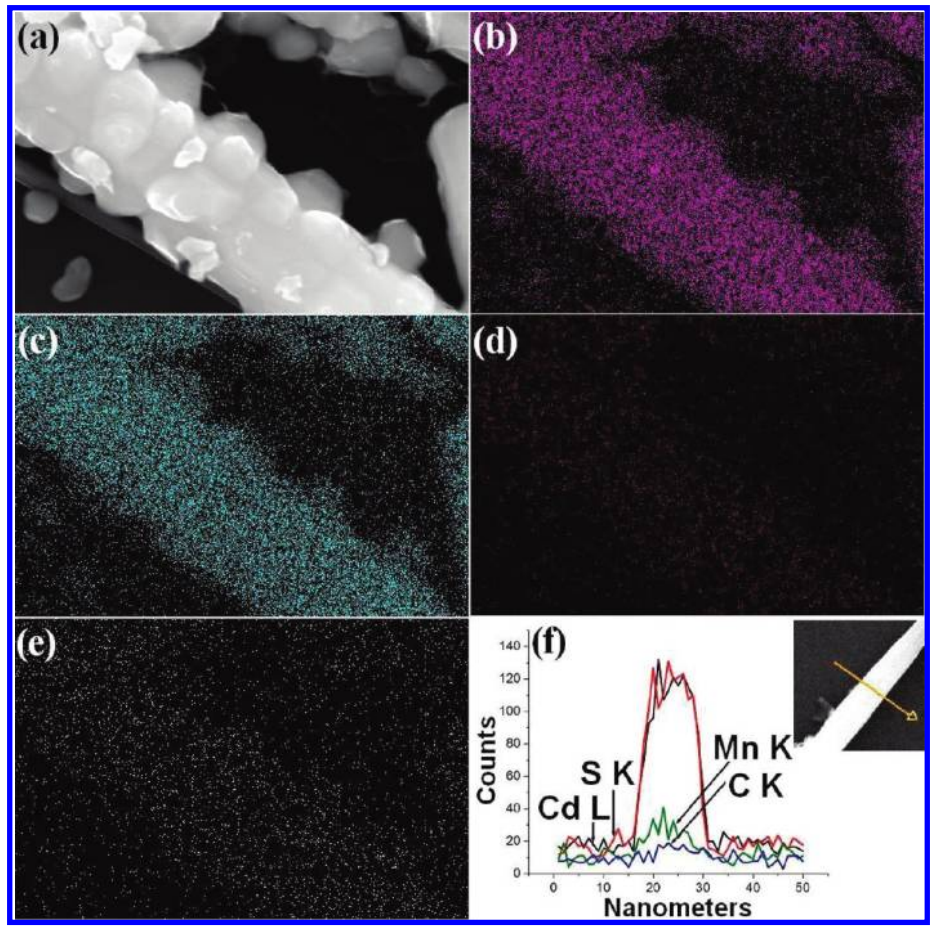

Figure 3. (a) Selected image of C2 for X-ray dot mapping. X-ray dot mapping for (b) Cd, (c) S, (d) Mn, and (e) C, on the selected (a) image. Elemental line scan of a nanorod in C5 (shown in the inset).

nanocrystals. The carbon shell (lighter contrast) was observed to be 7−11 nm in thickness (Figure 2a,b,e−g), which is enough to protect the DMS core. The $Cd_{1-x}Mn_xS$ nanocrystal core is 38 ± 5 and 43 ± 8 nm, in C0 and C1, respectively. Nanocrystals in C2 consisted of 34−54 nm square and tetrahedral nanocrystals (Figure 2c), as well as tripod nanostructures (Figure 2d), with tripod branches being ∼62 nm wide, which very well matched the HRSEM observations. Similarly, incomplete growth of the nanorods in C3 was observed in TEM (Figure 2e,f). The inset of Figure 2g shows a fully grown 52 nm thick nanorod, and the hexagonal nanocrystals are ∼59 nm thick (Figure 2g). As observed in HRSEM, TEM images of the C5 sample also showed nanorods with an aspect ratio of ∼32. Thus, the morphological studies definitely establish a trend in the shape of the $Cd_{1-x}Mn_xS$/C nanocrystals with the change in the Mn/Cd atomic ratio. As reported in the literature, $Cd_{1-x}Mn_xS$ nanowires and nanorods were earlier grown either by the catalytic effect of foreign Au nanoparticles in the solution phase[2a] or by chemical vapor deposition,[17] within porous silica templates,[18] or by hydrothermal synthesis inside an autoclave.[19] In this system, Mn might act as the catalyst in the formation of the nanorods.

Elemental dot mapping of a nanorod in C2 was performed with a highly sensitive, wave-dispersive X-ray analyzer (WDX) coupled to the HRSEM instrument to determine the microscopic bulk composition of the nanocrystals. Figure 3a shows a section of the nanorod, and the contents of Cd, S, Mn, and C are observed in Figure 3b−e, respectively. The Cd, S, and Mn signals were detected within the position of the nanorod. The sample was dispersed on a Si wafer. In fact, manganese was found to be uniformly distributed within the nanorods and nanocrystals, without any observable formation of heterogeneous Mn^{2+}−Mn^{2+} clusters. The overlapping carbon signal was observed everywhere within the sample region, which confirmed the encapsulating carbon shell over the $Cd_{1-x}Mn_xS$ nanocrystal core. The elemental line scanning of a nanorod in C5 (placed on a Si wafer, Figure 3f, inset) showed a huge, nearly equal, rise in concentration of the Cd L and S K lines and a relatively weaker Mn K intensity, owing to 4.5 atomic % of Mn in C5. The low intensity of the C K line is due to the ∼10 nm encapsulating carbon shell. The core−shell nanocrystals were formed by a one-step, template-free, kinetically controlled process. At high temperature and pressure inside the closed reactor, the Cd- and Mn-acetates decompose and atomize into their gaseous state atoms, along with gaseous sulfur. The decomposition follows the similar steps as reported previously.[11] Sulfur evaporates above 717 °C and reacts with $(Cd_{1-x}Mn_x)$−O to form $Cd_{1-x}Mn_xS$ via the following reaction: $2Cd_{1-x}Mn_xO + 2S \rightarrow 2Cd_{1-x}Mn_xS + O_2$. All the products of the dissociation reaction are formed in the gas phase, followed by solidification into the core−shell morphology. The solidification rate of $Cd_{1-x}Mn_xS$ is faster than carbon, and hence, $Cd_{1-x}Mn_xS$ crystallizes initially to form the core, followed by carbon, giving rise to the core−shell structure. A little stoichiometric excess of S was added to eliminate small percentages of $Cd_{1-x}Mn_xO$ and Mn-oxide impurity phases. The gas-phase reaction permits a perfect mixing of the reactants for the synthesis of a homogeneous distribution of manganese in the CdS matrix.

The XRD patterns of the $Cd_{1-x}Mn_xS$/C products are shown in Figure 4. All the reflection peaks in the products could be

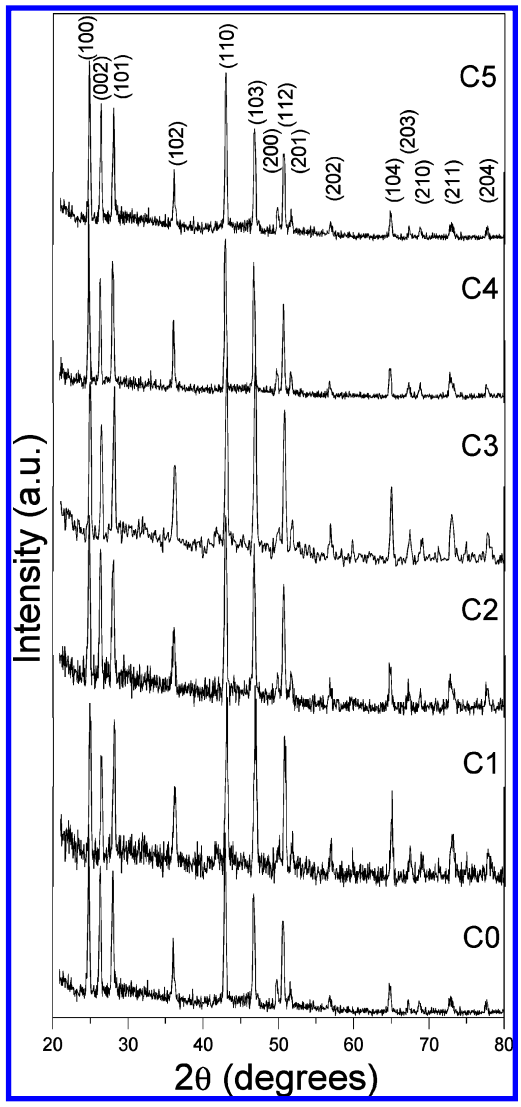

Figure 4. XRD patterns of the CdS:Mn^{2+}/C nanocrystals.

readily indexed to the hexagonal CdS (*P*63*mc* space group), which agree well with the reported data in JCPDS card no. 41-1049. Typical (002) reflections of graphitic carbon were not observed around $2\theta \simeq 26.4°$, probably due to the amorphous or semicrystalline nature of the encapsulating shell. The reaction conditions were controlled and optimized to eliminate any impurity phase formation, such as Cd-oxide, Mn-oxide, and metallic sulfur, and such peaks are not detected in the XRD patterns. In particular, diffraction peaks from any of the MnS phases were also absent in the XRD patterns. However, the relative intensities of (100), (101), (110), and (103) reflections were observed to vary with the increase in Mn concentration in the nanocrystals. This might occur due to the replacement of Cd^{2+} by Mn^{2+} at different lattice sites of the $Cd_{1-x}Mn_xS$ lattice. We did not observe any significant shift of the major XRD reflections for the different samples. XRD studies indicate the occupancy of the Cd^{2+} by Mn^{2+}, so the crystal structure of pristine CdS is retained in all the nanocrystals.

Raman Spectroscopy. The changes in the atomic arrangement of the CdS lattice due to the Mn^{2+} doping and the nature of the carbon shell were probed by Raman scattering experiments. Figure 5 shows the room-temperature Raman spectra of the representative C0 and C5 products, where 100−650 and 1000−1900 cm^{-1} correspond to the spectral regions of the $Cd_{1-x}Mn_xS$ core and carbon shell, respectively. In the 100−650 cm^{-1} region for C0, the Raman peaks are observed at 282−298 and 578−581 cm^{-1}, which are attributed to the first harmonic (1LO) and second harmonic (2LO) longitudinal optic phonon modes of CdS, respectively.[20] The LO modes are shifted as compared with the reported 1LO (300−305 cm^{-1}), and 2LO (600 cm^{-1}) modes for quantum dots, bulk, and thin film samples of CdS.[20,21] A continuous shift of the 1LO and 2LO phonon energies was observed from 298 cm^{-1} (C0) to 282 cm^{-1} (C5), as a function of increasing Mn concentration in the nanocrystals. In the $Cd_{1-x}Mn_xS$/C nanocrystals, due to a higher surface-to-volume ratio as compared with that of bulk CdS, there is an increase in the number of atoms at the surface compared with the interior of the nanocrystals, although, for ∼50 nm nanocrystals, the number of surface atoms is very few. In any case, the surface atoms are bound by weaker van der Waal's forces to the carbon atoms at the nanocrystal surface, and hence, the vibrational frequency is lower than the interior atoms, as observed by a decrease in the phonon energies in C0 and the doped nanocrystals.[22] However, with Mn^{2+} doping, there is an additional factor of lattice softening because Mn^{2+} replaces the Cd^{2+} sites, leading to the overall shift of the Raman modes toward lower phonon energies. In the 1000−1900 cm^{-1} spectral region, the distinct peaks at 1323 and 1590 cm^{-1} correspond to the D (Raman-inactive A_{1g} vibration mode of disordered graphite) and G (Raman-active optical E_{2g} mode of 2D graphite) bands of the carbon shell.[11] As observed, the I_D/I_G ratios are 1.2, and 1.1 for C0 and C5, respectively, implying the presence of a majority of disordered carbon at the shell of the $Cd_{1-x}Mn_xS$/C nanocrystals.

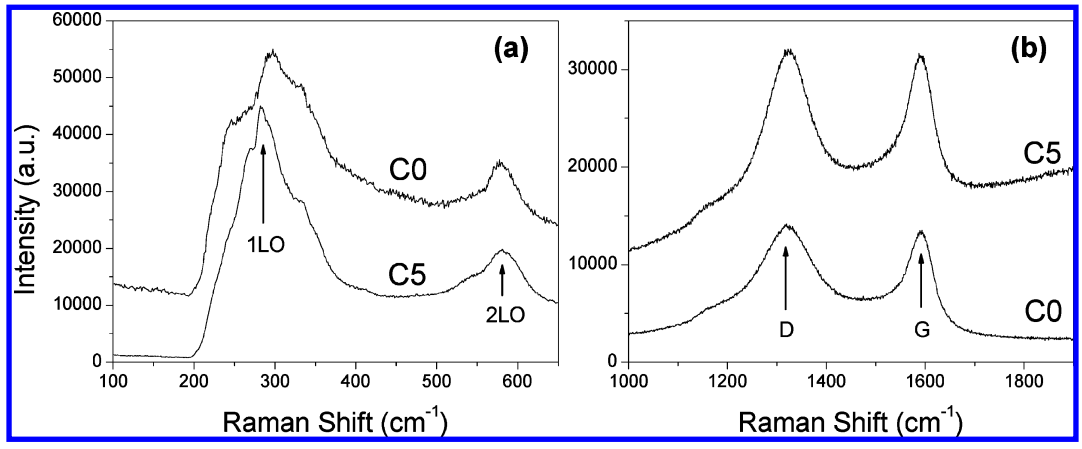

Figure 5. Raman spectra of (a) the CdS:Mn^{2+} nanocrystal core and (b) the carbon shell.

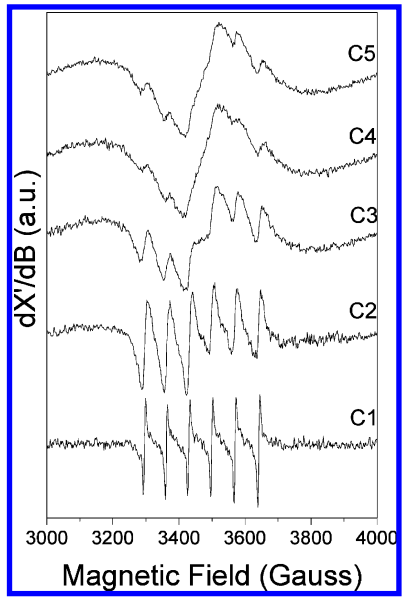

Figure 6. EPR spectra of CdS:Mn^{2+}/C at 300 K.

EPR Studies. EPR hyperfine splitting acts as a sensitive probe for the local environment of manganese. EPR experiments were performed at room temperature to envisage the location of Mn at different possible sites, core or surface, substitutional or interstitial site, present in the nanocrystals.[23] At 300 K, six-line EPR spectra arise due to the hyperfine interaction from the ^{55}Mn nucleus ($I = 5/2$) and correspond to the allowed transition ($\Delta m_s = \pm 1$, $\Delta m_I = 0$), where m_s and m_I are the electron spin and nuclear spin quantum numbers, respectively.[24] In Figure 6, the spectra of C1 and C2 exhibit the expected sextuplet, whereas for C3, a broad resonance creeps up in the middle of the six-line spectrum. For higher doping (C4 and C5), the interactions between the spins lead to a broad resonance that overlaps the sextuplet, indicating the domination of $Mn^{2+}-Mn^{2+}$ exchange and dipolar interactions. We determined a hyperfine splitting constant (A) of 64.8×10^{-4}, 64.1×10^{-4}, and 66.2×10^{-4} cm^{-1} for C1, C2, and C3, respectively, at 300 K. With an increase in Mn concentration, the changes in the coordination environment of Mn^{2+} modify the crystal field, leading to an enhancement in the hyperfine splitting, and less coupling between the ground state of Mn and sp states of the nanocrystals, which sometimes results in a total collapse of the hyperfine interaction of the Mn^{2+} nucleus.[12,23] For all the samples, the gyromagnetic value found is typical of Mn^{2+} species ($g_0 = 2.000$). The EPR studies conclude that, for all doped samples, the dopant is present in the +II oxidation state. Hence, we assume that Mn^{2+} is efficiently doped within the CdS host lattice for C1 and C2. In C3, there is a chance of the presence of very small Mn clusters and partial segregation of Mn^{2+} at the surface of the CdS nanocrystals, where a fraction of Mn^{2+} might still be embedded inside the nanocrystal core, as will be shown in the CL results below. For higher doping, Mn has a tendency to form pairs and/or clusters, which masks the hyperfine interactions. Unlike our earlier study on Mn^{2+} doping into wurtzite CdSe nanocrystals, where Mn^{2+} was efficiently doped until a Mn:Cd atomic ratio of 0.099,[23] CdS nanocrystals could be efficiently doped only up to 1.2 atomic % manganese (C2) using the same synthesis approach. In fact, it is reported in the literature that Mn^{2+} can be successfully doped into the nanocrystals having a zinc-blende crystal structure, whereas the wurtzite nanocrystals have not been successfully doped, or only up to a low concentration (1%) of manganese.[24]

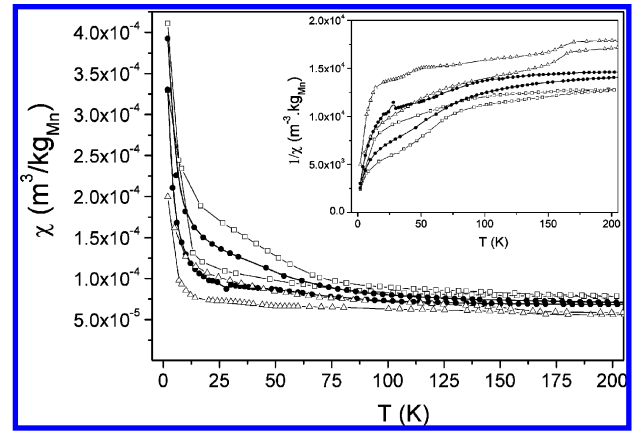

Figure 7. Magnetic susceptibilities and inverse susceptibilities (inset) for samples C1 (squares), C3 (dots), and C5 (triangles).

Magnetic Characterization. The magnetic properties were studied as a function of manganese concentration for all samples, but only three samples (C1, C3, and C5) are reported for clarity. The magnetic susceptibility was investigated using a zero-field-cooled/field-cooled (ZFC/FC) routine at a field of $\mu_0 H = 0.02$ T. Figure 7 shows the susceptibility plotted as a function of temperature and, in the inset, as a function of inverse temperature. The magnetic susceptibility χ has been plotted per mass of Mn and hardly depends on dopant concentration. For all samples, the curve presents a large irreversibility between the ZFC and FC curves for the temperature range from 2 to 300 K. Plots have been recorded until 300 K but are shown only up to 200 K to enhance the low-temperature features for the reader; from 200 to 300 K; χ does not display any interesting features. The susceptibility could be analyzed as resulting from three phenomena: (i) a paramagnetic behavior (obvious for $T < 20$ K), (ii) localized antiferromagnetic interactions (bumps from 25 to 75 K, and even up to 160 K for C1), and (iii) ferromagnetic behavior, as we can see from a χ constant value above 160 K. The $1/\chi$ plots clearly show the curvy bumps from 25 to 75 K and at 160 K. They cannot be ascribed to any magnetic transition known for any of the hypothetic impurities (MnS, MnO, and related compounds); this behavior might then be a signature of localized short-range magnetic ordering at lower temperatures.[25]

From the magnetization (M) plot as a function of applied magnetic field $\mu_0 H$ (T) at 300 K in Figure 8a, it is evident that all the $Cd_{1-x}Mn_xS$/C samples are not purely paramagnetic at room temperature and present a hysteresis, which is a signature of predominant ferromagnetic interactions for C1−C5 nanocrystals. Moreover, a smaller nanocrystal size can give rise to superparamagnetic fractions at room temperature. In fact, when the particle size is reduced to several nanometers, both antiferromagnetic and ferromagnetic systems can display superparamagnetism.[26] The results from the high-field $M(H)$ measurements at low temperature ($T = 2$ K) are plotted in Figure 8b. Even at 2 K and an applied field of 6 T, none of the samples display saturation of the magnetic moment. The coercive field values at 2 K are $\mu_0 H = 7.1$, 4.0, and 3.5 mT for C1, C3, and C5, respectively. The magnetic moments follow a Langevin function $M(H,T) = M_T L(\mu H/k_B T)$, and the hysteresis loops are plotted in Bohr magnetons per manganese atoms. The expected magnetic moment of a free Mn atom in the +II valence state is 5.92 μ_B, accounting for the spin contributions. The Langevin fit to the hysteresis loops at 2 K gives lower values of 4.43 ± 0.04 μ_B/Mn (C1), 4.52 ± 0.04 μ_B/Mn (C3), and 2.85 ± 0.03 μ_B/Mn (C5), explained by the coexistence of antiferromagnetic interactions between the second neighbor Mn spins through

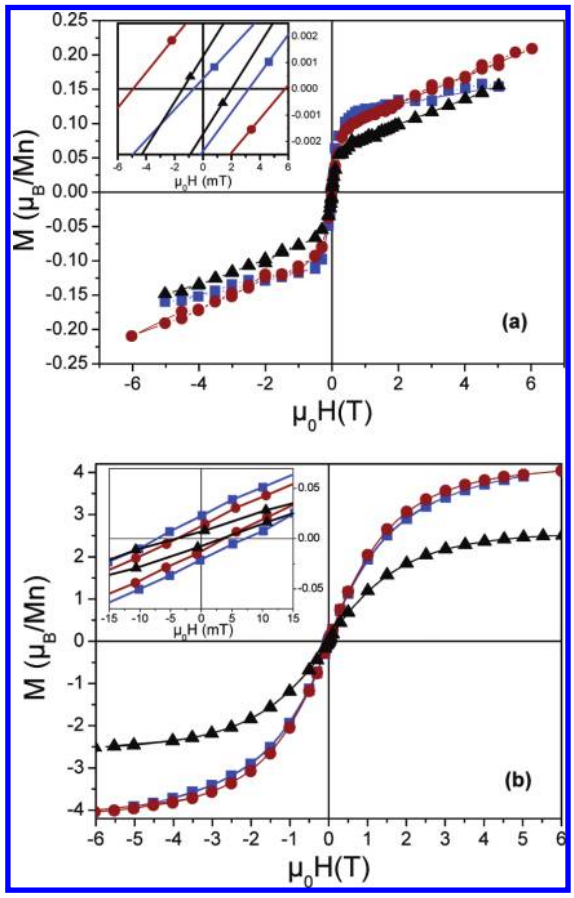

Figure 8. Magnetization curves at (a) 300 and (b) 2 K, for samples C1 (squares), C3 (dots), and C5 (triangles). Insets show the respective coercive fields.

indirect Mn−S−Mn exchange.[27] Both EPR and magnetic studies are consistent with the +II state of manganese in the nanocrystals along with the occurrence of magnetic interactions.

It is to be noted here that the observed ferromagnetic behavior is not due to any contaminations in the samples, which have been ruled out by careful ICP measurements. Ferromagnetism has been previously observed in $Cd_{1-x}Mn_xS$ nanostructures, although the exact origin of ferromagnetism in Mn-doped II−VI semiconductors is still uncertain.[7,28] In our case, μ_B/Mn decreases with the increase in Mn^{2+} concentration in the nanocrystals. These observations are relative to the local structures of Mn^{2+} ions in the CdS matrix due to different doping concentrations. At lower Mn^{2+} concentrations (C1 and C3), isolated Mn^{2+} ions exist in the partially substituted CdS:Mn^{2+} lattice, whereby ferromagnetic coupling between the isolated Mn^{2+} spins is the only collective phenomenon that was observed, apart from a paramagnetic contribution from free spins. In C3−C5, Mn^{2+} spins are also interacting through indirect exchange coupling, sulfur mediating the antiparallel ordering of two Mn^{2+} spins. This explains both the lowering of the magnetic moment observed in SQUID measurements and the appearance of a broad background signal in EPR studies, with the increase in Mn^{2+} doping. However, at the doping levels studied, the average distance of the Mn^{2+} ions is just less than 13 Å,[29] which is too large as expected for any indirect exchange in a homogeneous compound. The antiferromagnetic behavior is, therefore, the signature of local heterogeneity in concentration. Moreover, additional charge transfer mediated ferromagnetism is likely to occur through the carbon shell via long-range coupling of the spins. Ferromagnetic interactions can also originate from the vacancies and defects present within the carbon shell over the nanocrystals.[30]

Cathodoluminescence Spectroscopy. Stack plots of the spatially integrated cathodoluminescence spectra for temperatures of 50−300 K are shown for samples C0−C5 in Figure 9a−e, respectively. In Figure 9a, the CdS NBE emission is apparent at ∼2.558 eV at low temperatures and gradually shifts toward ∼2.458 eV at room temperature, consistent with the temperature dependence of the band gap. In addition, a broad and intense defect- or surface-related emission centered at ∼2.26 eV is observed at $T = 50$ K. To identify its origin with greater certainty, we have decomposed the spectra of Figure 9a into two Gaussian components. At 50 K in Figure 9a, the decomposition yields NBE and a separate component labeled as *S*. For each of the samples in Figure 9a−e, only the fits for $T =$ 50, 150, and 300 K are shown, to illustrate typical results of the fits in order to conserve on space. Additional aspects of the fits are presented in Figure 9f in which a table indicating the average full width at half-maxima (fwhm) of the NBE, *P*, *S*, and *S′* components (defined below) and the average adjusted R^2 of the fits are shown, where the average is taken over all fits in the 50−300 K range for a given sample. The standard deviation (σ) for each average fwhm is also shown in the table. The standard deviations range typically from ∼10 to 20% of the average fwhm and indicate a relatively small variation in the width of each component when averaged over all temperatures. The energy and the intensity of the decomposed NBE and *S* components are shown in Figure 10a. Whereas the energy of the NBE component gradually shifts toward lower energy with increasing temperature, the *S* component remains roughly constant in energy over the 50 to ∼180 K range before it shifts toward higher energy by about ∼60 meV. The dissimilar temperature-dependent trends exhibited by the NBE and *S* component emissions suggest that the *S* component is not derived from a bulk impurity or defect state but rather from a surface state related emission process. A similar surface-related emission band has been reported for undoped CdS nanocrystals.[31]

From the temperature dependence of the CL intensities in Figure 10a for C0, the NBE emission decreases gradually by ∼40% as the temperature increases from 50 to 300 K. Over the same temperature range, the *S* component intensity is observed to decrease monotonically by a factor of ∼7. The more rapid decrease of the *S* component intensity over the 50−300 K temperature range in comparison with that for the NBE component suggests that thermal excitation at higher temperatures leads to a substantial reduction in excess carriers that recombine radiatively near surface traps and defect states at the nanocrystal surface. The result is a pronounced NBE peak that is observed in all the CL spectra of Figure 9 at $T = 300$ K.

The CL spectra of Figure 9b,c show subtle changes at $T =$ 50 K with Mn dopings of 0.4% (C1) and 0.6% (C2). For both doping concentrations, the CdS NBE emission at $T = 50$ K is noticeably absent. Also, in C2 (Figure 9c), the sub-band-gap emission becomes noticeably asymmetrical with a sharp peak and shoulder at ∼2.2 and ∼2.4 eV, respectively. The lower energy emission is evidently due to the Mn^{2+} intra d-shell $^4T_1 \rightarrow {}^6A_1$ transition.[3,32] The optical activity is consistent with an incorporation of Mn^{2+} ions in the host nanocrystal, as evidenced by the EPR spectra of C1 and C2 in Figure 6, which exhibit the expected sextuplet. To more accurately ascertain the position of the Mn^{2+} intra d-shell $^4T_1 \rightarrow {}^6A_1$ transition, we have used a three-component fit for the CL spectra of C2 in Figure 9c, for which *P*, *S′*, and NBE are used to label the three Gaussian

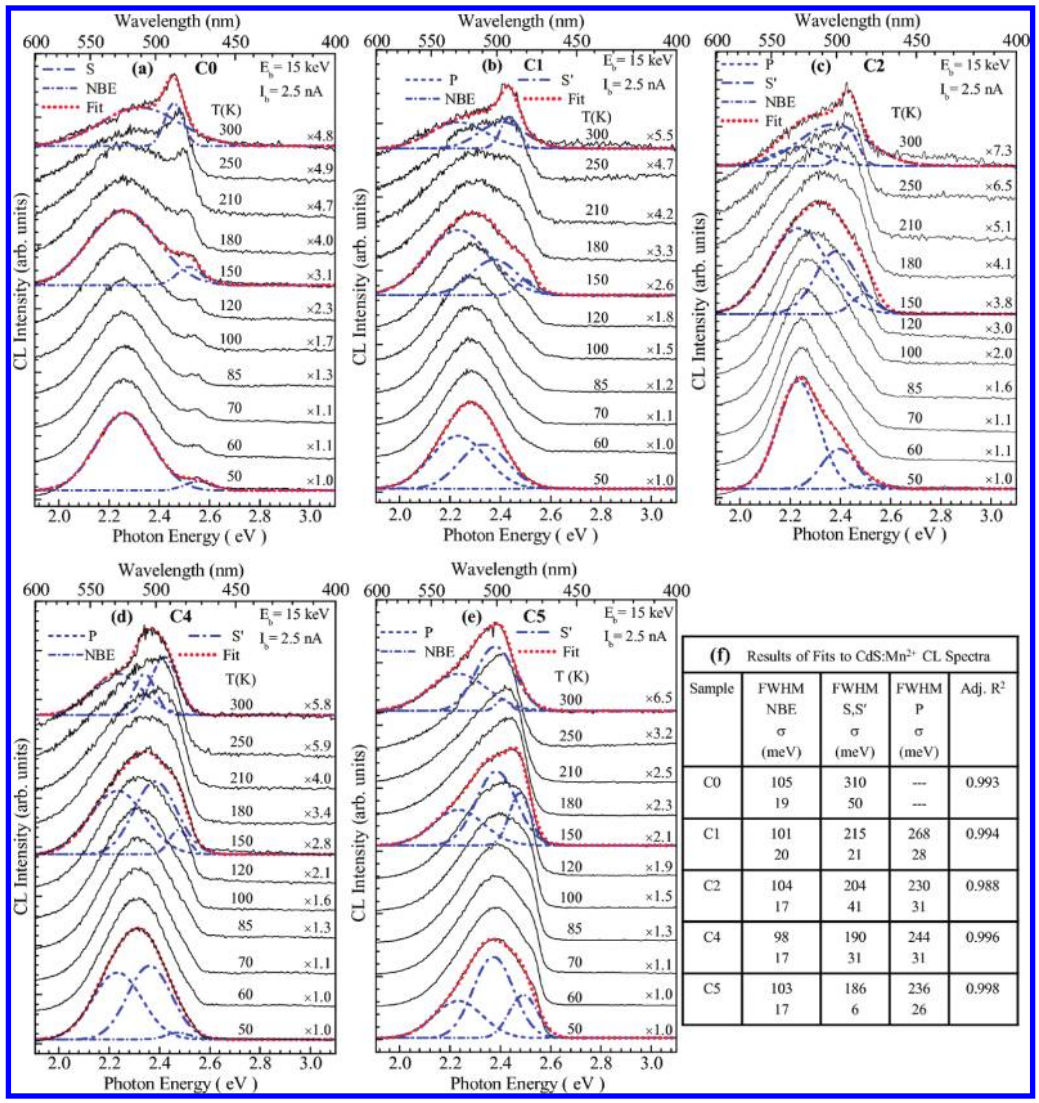

Sample	FWHM NBE σ (meV)	FWHM S,S' σ (meV)	FWHM P σ (meV)	Adj. R^2
C0	105 19	310 50	--- ---	0.993
C1	101 20	215 21	268 28	0.994
C2	104 17	204 41	230 31	0.988
C4	98 17	190 31	244 31	0.996
C5	103 17	186 6	236 26	0.998

Figure 9. Spatially integrated CL spectra for various temperatures in the 50−300 K temperature range for samples C0, C1, C2, C4, and C5 in (a)−(e). The spectra were decomposed into Gaussian components, as illustrated for each sample for the components plotted under the spectra for $T = 50$, 150, and 300 K. The table in (f) shows the average fwhm of the components NBE, *S*, *S*′, and *P*; the standard deviation (σ) of the fwhm; and the adjusted R^2 of the fits. The fwhm and σ are determined by averaging over all temperatures in the 50−300 K range for each sample.

components. The fit for $T = 50$ K yielded the results displayed beneath the bottom spectrum in Figure 9c. The energy positions of the *P* and *S*′ components are 2.233 and 2.396 eV, respectively. The energy of the *P* component is consistent with that of the Mn^{2+} intra d-shell $^4T_1 \rightarrow {}^6A_1$ transition,[3,32] whose energy varies much more slowly than the NBE peak as the sample temperature is increased from 50 to 300 K. To more accurately track the temperature-dependent variations of the *S*′ and *P* components, we have constrained the *P* component to its $T = 50$ K value of 2.233 eV for the remaining CL spectra of C2 in Figure 9c, as well as for the entire set of CL spectra for C1, C4, and C5 in Figure 9. Our hypothesis is that, because the *P* component emission reflects the emission of Mn^{2+} incorporated in the bulk part of the nanocrystal, it should remain approximately independent of the Mn^{2+} doping density. Moreover, the Mn^{2+} transition energy is relatively independent of temperature and is expected to vary, at most, on the order of ∼10 meV from 50 to 300 K, as observed in the similar ZnSe:Mn^{2+} system.[13]

The results of the fits are shown for C1, C2, and C5 in Figure 10b−d. Again, it is apparent that the energy position of the *S*′ component does not follow the energy position of the NBE as the temperature is varied from 50 to 300 K, thus precluding its origin as a bulk CdS impurity- or defect-related feature. Rather, *S*′ likely originates from clusters of Mn^{2+} (as evidenced from the EPR results) where the density of segregated Mn^{2+} grows in the sample sequence of C1−C5. Previous optical measurements of $Zn_{1-x}Mn_xTe$ have demonstrated that an increasing Mn concentration, *x*, from 0 to 1 leads to an increase of ∼100 meV in the intra-Mn^{2+} luminescence energy, as local modifications of the crystal field environment accompany an increased Mn^{2+} concentration.[14] Figure 10b−d reveals an approximate blue shift of ∼100 to 170 meV in the *S*′ component relative to *P*, again consistent with an increase in the intra d-shell Mn^{2+} transition energy that can be expected for manganese clusters at the surface. Moreover, Figures 9 and 10 show an increase in the *S*′-to-*P* intensity ratio for $T = 50$ K as the Mn concentration increases in the sample sequence of C2−C5. It is worth noting that the *S*′ peak for sample C1 originates predominantly from surface state transitions associated with a Mn-free surface, as most of the Mn^{2+} is likely incorporated in the bulk of the host nanocrystal for a 0.4% Mn concentration. However, we cannot rule out the presence of a small fraction of Mn in clusters at the surface that could disproportionately affect the optical

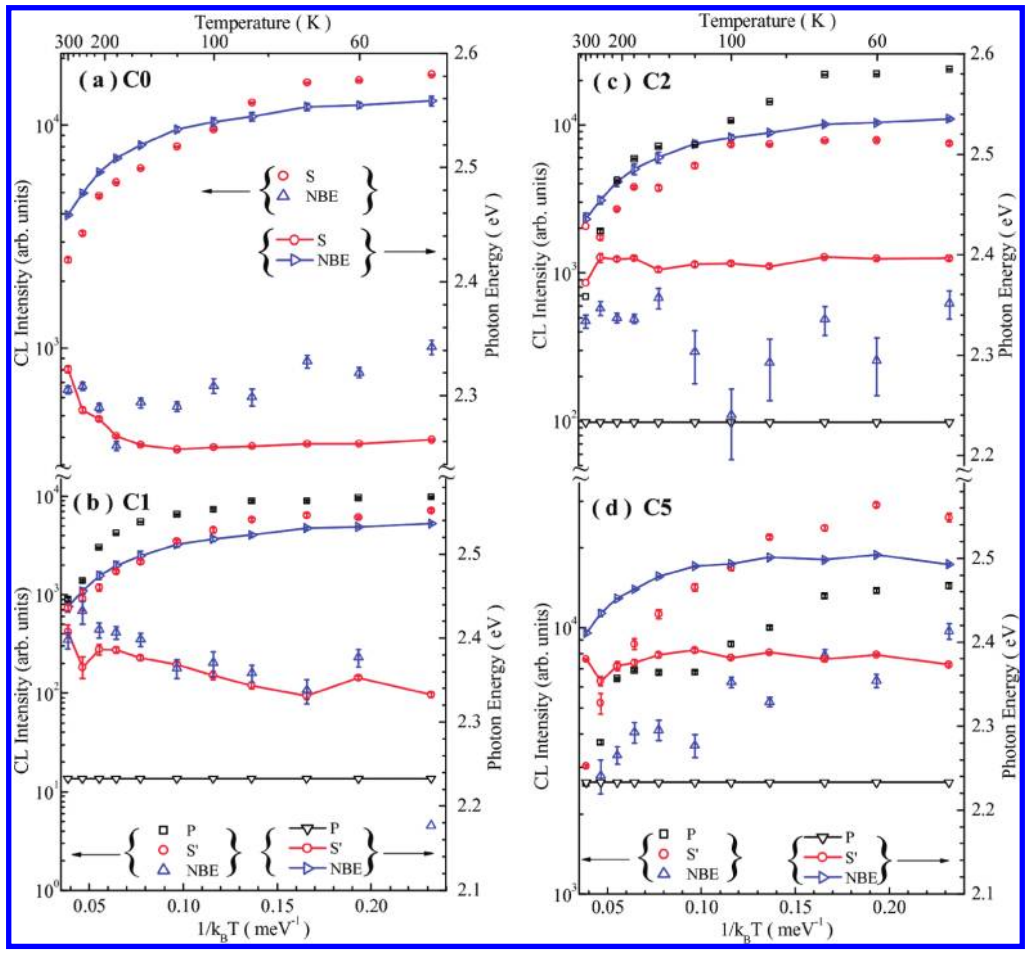

Figure 10. CL intensity and energy of the Gaussian components *S*, *S′*, *P*, and NBE that were obtained from the fits shown partially in Figure 9. The results are shown for various temperatures in the 50−300 K range. Error bars for the fitting results are shown and observed to be inside some of the open symbols.

activity and lead to an∼70 meV energy shift in *S′* relative to *S*, as observed in Figure 10a,b for $T = 50$ K.

The increase in the NBE emission intensity with temperature from 50 to 300 K by a factor of ∼4 for C1 is to be compared with the ∼40% decrease in the NBE intensity for C0 (Figure 10a,b) over the same temperature range. This difference is attributed to the presence of the well-incorporated 0.4% Mn doping in C1, which leads to a more efficient energy transfer from the host CdS crystal to the Mn^{2+} ions and a reduced relative NBE emission intensity as the temperature decreases to 50 K in C1. This increase in the Mn^{2+} intra d-shell $^4T_1 \rightarrow {}^6A_1$ transition is ascribed to a more efficient energy transfer from CdS to Mn^{2+}, as also evidenced by the increase in the *S′*-to-*P* intensity ratio for $T = 50$ K as the Mn concentration increases in the sample sequence of C2−C5. Thus, thermal energy is essential in determining the relative probability of energy transfer from the host crystal to the Mn ion before the intra d-shell Mn^{2+} radiative recombination occurs. Therefore, the reduced relative NBE emission intensity at low temperatures for C1 and C2 in Figure 9b,c, the pronounced *P* emission for C2, and again the sharp sextuplet spectra in the EPR spectra of Figure 6 all further underscore that Mn^{2+} is well incorporated in the crystal and leads to an efficient energy transfer and optical activity.

Finally, we have examined the effects of the carbon shell on the optical activity the nanocrystals by examining a particular sample of CdS:Mn^{2+} nanocrystals that was synthesized without the carbon shell. The ∼25 nm nanocrystals contained 1.2 wt % Mn (i.e., with the same approximate Mn concentration as the C4 sample with the carbon shell). We show in Figure 11 a stack plot of the CL spectra acquired for this sample for various temperatures from 50 to 300 K. As for the CL spectra for the carbon-encapsulated samples, we have decomposed the spectra into components that clearly show the NBE and a lower-energy feature at ∼2.1 eV, consistent with the Mn^{2+} intra d-shell $^4T_1 \rightarrow {}^6A_1$ transition. Thus, for the nonencapsulated (bare) sample, only two components are reliably observed in the CL spectra at low temperatures, and so we have fit the spectra by assuming a two-component fit. The results of the fits are shown in the spectra for 50, 100, and 150 K in Figure 11. The presence of the *P* component at ∼2.1 eV is consistent again with the Mn^{2+} intra d-shell $^4T_1 \rightarrow {}^6A_1$ transition. However, we observe no clear surface features or features associated with Mn^{2+} clusters in the 50−150 K temperature range. In striking contrast to the carbon-encapsulated nanocrystals, the luminescence intensity decreases rapidly with temperature for temperatures greater than ∼150 K, as observed in Figure 11. The emission intensity of the NBE feature for the bare sample is about 3 orders of magnitude lower at 300 K, in comparison with the CL spectrum at 50 K. In contrast, the five carbon-encapsulated samples, C0−C5, exhibited a decrease in total emission intensity by less than an order of magnitude as the temperature was increased from 50 to 300 K, as observed in Figure 9. Moreover, in the bare sample, a pronounced lower-energy band near ∼1.8 eV emerges and grows for temperatures above ∼150 K, indicating the presence of bulk or surface-related defect features. Thus,

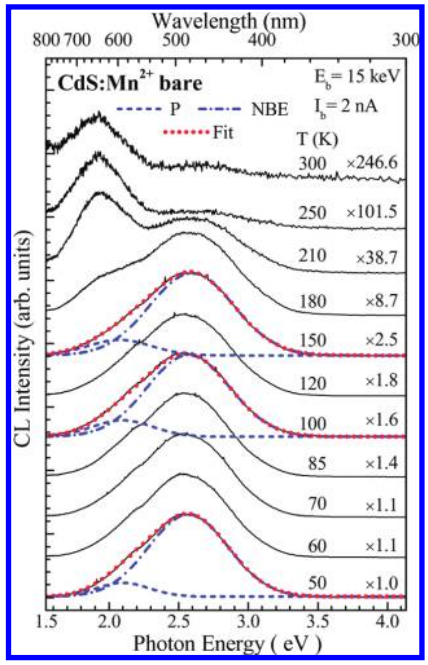

Figure 11. Spatially integrated CL spectra for various temperatures in the 50−300 K temperature range for the bare CdS:Mn^{2+} nanocrystal sample (i.e., without carbon encapsulation). The weight percent of Mn is ∼1.2% and corresponds to the C4 sample with carbon encapsulation. The spectra were decomposed into Gaussian components, as illustrated for the components plotted under the spectra for $T = 50$, 100, and 150 K.

the combination of these defect features and a markedly reduced luminescence efficiency with a high nonradiative recombination rate near room temperature in the bare CdS sample attests to the importance of carbon encapsulation of the nanocrystals in (i) passivating the nanocrystal surface and (ii) observing measurable NBE- and Mn^{2+}-related luminescence at room temperature.

Conclusions

In conclusion, carbon-encapsulated CdS:Mn^{2+} nanocrystals with a Mn atomic % of 0, 0.9, 1.2, 1.8, 2.4, and 4.5 were synthesized by the one-step, solid-state reaction inside a closed reactor at 800 °C. The mechanism for the formation of the ∼50 nm $Cd_{1-x}Mn_xS$ nucleus core, encapsulated by a 5−11 nm thick disordered carbon shell, without the use of any template, is a kinetically controlled process. The $Cd_{1-x}Mn_xS$ core has a hexagonal wurtzite structure. The nanorods were formed with higher Mn^{2+} doping, as a result of the catalytic action of the segregated manganese. Mn^{2+} is efficiently and uniformly doped inside the CdS core until a Mn/Cd atomic ratio of 0.012, as evidenced from the room-temperature EPR measurements. For more concentrated samples, EPR and SQUID measurements are consistent with the presence of clusters with antiferromagnetic interactions. Ferromagnetism was observed for all the doped samples, the magnetic moment being highest in the 0.4 and 0.6% doped samples. The optical properties have been studied with variable-temperature cathodoluminescence. The incorporation of Mn^{2+} into the host nanocrystal was studied by examining variations in the CdS near band edge (NBE) emission intensity, the Mn^{2+} intra d-shell $^4T_1 \rightarrow {}^6A_1$ emission intensity, and defect-related surface state transitions as a function of temperature. The changes in luminescence intensity and energy of the various spectral features as a function of Mn^{2+} concentration were quantified from the CL spectra in the 50−300 K range. The pronounced intra Mn^{2+} emission further consolidates the efficient incorporation of Mn^{2+} in the CdS nanocrystal, resulting in an efficient energy transfer from the host CdS crystal to the Mn^{2+} ion and its resulting d-shell $^4T_1 \rightarrow {}^6A_1$ optical emission.

References and Notes

(1) (a) Wolf, S. A.; Awschalom, D. D.; Buhrman, R. A.; Daughton, J. M.; von Molnár, S.; Roukes, M. L.; Chtchelkanova, A. Y.; Treger, D. M. *Science* **2001**, *294*, 1488–1495. (b) Ohno, H. *Science* **1998**, *281*, 951–956. (c) Dietl, T.; Ohno, H.; Matsukura, F.; Cibert, J.; Ferrand, D. *Science* **2000**, *287*, 1019–1022.

(2) (a) Delikanli, S.; He, S.; Qin, Y.; Zhang, P.; Zeng, H.; Zhang, H.; Swihart, M. *Appl. Phys. Lett.* **2008**, *93*, 132501. (b) Ishizumi, A.; Kanemitsu, Y. *Adv. Mater.* **2006**, *18*, 1083–1085. (c) Yang, H.; Holloway, P. H. *Adv. Funct. Mater.* **2004**, *14*, 152–156.

(3) Chandramohan, S.; Kanjilal, A.; Tripathi, J. K.; Sarangi, S. N.; Sathyamoorthy, R.; Som, T. *J. Appl. Phys.* **2009**, *105*, 123507.

(4) Chen, D.; Viswanatha, R.; Ong, G. L.; Xie, R.; Balasubramaninan, M.; Peng, X. *J. Am. Chem. Soc.* **2009**, *131*, 9333–9339.

(5) Dantas, N. O.; Neto, E. S. F.; Silva, R. S.; Jesus, D. R.; Pelegrini, F. *Appl. Phys. Lett.* **2008**, *93*, 193115.

(6) (a) Taguchi, S.; Ishizumi, A.; Tayagaki, T.; Kanemitsu, Y. *Appl. Phys. Lett.* **2009**, *94*, 173101. (b) Kar, S.; Santra, S.; Heinrich, H. *J. Phys. Chem. C* **2008**, *112*, 4036–4041.

(7) Xue, H. T.; Zhao, P. Q. *J. Phys. D: Appl. Phys.* **2009**, *42*, 015402.

(8) Ishizumi, A.; Matsuda, K.; Saiki, T.; White, C. W.; Kanemitsu, Y. *Appl. Phys. Lett.* **2005**, *87*, 133104.

(9) (a) Keshari, A. K.; Pandey, A. C. *J. Appl. Phys.* **2009**, *105*, 064315. (b) Ma, N.; Tikhomirov, G.; Kelley, S. O. *Acc. Chem. Res.* **2010**, *43*, 173–180.

(10) Guo, Y.; Wang, H.; He, C.; Qiu, L.; Cao, X. *Langmuir* **2009**, *25*, 4678–4684.

(11) Bhattacharyya, S.; Perelshtein, I.; Moshe, O.; Rich, D. H.; Gedanken, A. *Adv. Funct. Mater.* **2008**, *18*, 1641–1653.

(12) Bhattacharyya, S.; Zitoun, D.; Estrin, Y.; Moshe, O.; Rich, D. H.; Gedanken, A. *Chem. Mater.* **2009**, *21*, 326–335.

(13) Nag, A.; Sapra, S.; Nagamani, C.; Sharma, A.; Pradhan, N.; Bhat, S. V.; Sarma, D. D. *Chem. Mater.* **2007**, *19*, 3252–3259.

(14) Lin, H. T.; Rich, D. H.; Konkar, A.; Chen, P.; Madhukar, A. *J. Appl. Phys.* **1997**, *81*, 3186–3195.

(15) Na, C. W.; Han, D. S.; Kim, D. S.; Kang, Y. J.; Lee, J. Y.; Park, J.; Oh, D. K.; Kim, K. S.; Kim, D. *J. Phys. Chem. B* **2006**, *110*, 6699–6704.

(16) Brieler, F. J.; Fröba, M.; Chen, L.; Klar, P. J.; Heimbrodt, W.; Nidda, H.-A. K. v.; Loidl, A. *Chem.—Eur. J.* **2002**, *8*, 185–194.

(17) Wang, Q. S.; Xu, Z. D.; Nie, Q. L.; Yue, L. H.; Chen, W. X.; Zheng, Y. F. *Solid State Commun.* **2004**, *130*, 607–611.

(18) Chuu, D.-S.; Chang, Y.-C.; Hsieh, C.-Y. *Thin Solid Films* **1997**, *304*, 28–35.

(19) Romčević, N.; Kostić, R.; Romčević, M.; Čomor, M. I.; Nedeljković, J. M. *J. Phys. D: Appl. Phys.* **2005**, *38*, 4321–4324.

(20) Yang, R. D.; Tripathy, S.; Tay, F. E. H.; Gan, L. M.; Chua, S. J. *J. Vac. Sci. Technol., B* **2003**, *21*, 984–988.

(21) Bhattacharyya, S.; Zitoun, D.; Gedanken, A. *J. Phys. Chem. B* **2008**, *112*, 7624–7630.

(22) Erwin, S. C.; Zu, L.; Haftel, M. I.; Efros, A. L.; Kennedy, T. A.; Norris, D. J. *Nature* **2005**, *436*, 91–94.

(23) Gajbhiye, N. S.; Bhattacharyya, S. *J. Appl. Phys.* **2007**, *101*, 113902.

(24) Néel, L. *Ann. Géophys.* **1949**, *5*, 99.

(25) Clavel, G.; Willinger, M. G.; Zitoun, D.; Pinna, N. *Eur. J. Inorg. Chem.* **2008**, *6*, 863–868.

(26) Dietl, T. *Nat. Mater.* **2003**, *2*, 646–648.

(27) Delikanli, S.; He, S.; Qin, Y.; Zhang, P.; Zeng, H.; Zhang, H.; Swihart, M. *Appl. Phys. Lett.* **2008**, *93*, 132501.

(28) Zhang, Y.; Talapatra, S.; Kar, S.; Vajtai, R.; Nayak, S. K.; Ajayan, P. M. *Phys. Rev. Lett.* **2007**, *99*, 107201.

(29) Liu, S. M.; Liu, F. Q.; Guo, H. Q.; Zhang, Z. H.; Wang, Z. G. *Solid State Commun.* **2000**, *115*, 615–618.

(30) Lee, Y. R.; Ramdas, A. K.; Aggarwal, R. L. *Phys. Rev. B* **1986**, *33*, 7383–7385.

(31) Suyver, J. F.; Wuister, S. F.; Kelly, J. J.; Meijerink, A. *Phys. Chem. Chem. Phys.* **2000**, *2*, 5445–5448.

(32) (a) Ando, K. *Phys. Rev. B* **1993**, *47*, 9350–9353. (b) Yu, Y.-M.; O, B.; Yoon, M.-Y.; Kim, J. B.; Choi, Y. D. *Thin Solid Films* **2003**, *426*, 265–270.

JP107083F